Structure and function of the ROR2 cysteine-rich domain in vertebrate noncanonical WNT5A signaling

Samuel C. Griffiths[1]†, Jia Tan[2]†, Armin Wagner[3], Levi Blazer[4], Jarret J. Adams[4], Sachdev S. Sidhu[4], Christian Siebold[1]*, Hsin-Yi Henry Ho[2]*

[1]Division of Structural Biology, Wellcome Centre for Human Genetics, University of Oxford, United Kingdom
[2]Department of Cell Biology and Human Anatomy, University of California, Davis, United States
[3]Science Division, Diamond Light Source, Harwell Science and Innovation Campus, Didcot, United Kingdom
[4]The Donnelly Centre, University of Toronto, Canada

†co-first authors
*co-corresponding authors

Abstract

The receptor tyrosine kinase ROR2 mediates noncanonical WNT5A signaling to orchestrate tissue morphogenetic processes, and dysfunction of the pathway causes Robinow syndrome, Brachydactyly B and metastatic diseases. The domain(s) and mechanisms required for ROR2 function, however, remain unclear. We solved the crystal structure of the extracellular cysteine-rich (CRD) and Kringle (Kr) domains of ROR2 and found that, unlike other CRDs, the ROR2 CRD lacks the signature hydrophobic pocket that binds lipids/lipid-modified proteins, such as WNTs, suggesting a novel mechanism of receptor action. Functionally, we showed that the ROR2 CRD, but not other domains, is required and minimally sufficient to promote WNT5A signaling, and Robinow mutations in the CRD and the adjacent Kr alter ROR2 function. Moreover, we demonstrated that the activity of the ROR2 CRD requires Frizzled receptors. Thus, ROR2 acts via its CRD to potentiate the function of a receptor supercomplex that includes Frizzleds to transduce WNT5A signals.

Introduction

ROR proteins make up an important branch of the receptor tyrosine kinase (RTK) superfamily, conserved from sponges to humans. Originally identified as orphan receptors based on sequence homology to other RTKs (hence the name Receptor tyrosine kinase-like Orphan Receptor), work over the past two decades has elucidated a critical role of the ROR RTK family in mediating noncanonical WNT5A signaling (Oishi et al., 2003, Mikels and Nusse, 2006, Ho et al., 2012, Green et al., 2008). Unlike canonical WNTs, which signal through β-catenin-dependent transcription to regulate cell proliferation and tissue fate, WNT5A signals noncanonically through β-catenin-independent mechanisms to induce cytoskeletal rearrangements and tissue morphogenetic changes (Veeman et al., 2003, Moon et al., 1993). The pathway is also of clinical significance, as mutations in WNT5A, the ROR family member ROR2, and the downstream signal transducers DISHEVELLED 1 (DVL1) and DVL3 have been reported to cause Robinow syndrome (RS), a congenital disorder characterized by systemic tissue shortening defects, including dwarfism, mesomelic limb shortening, brachydactyly, genitourinary defects, cleft palate and other craniofacial dysmorphisms (Person et al., 2010, Afzal et al., 2000, van Bokhoven et al., 2000, Bunn et al., 2015, White et al., 2015, White et al., 2016). A distinct cohort of ROR2 missense mutations cause brachydactyly type B (BDB) (Oldridge et al., 2000, Schwabe et al., 2000). Moreover, elevated expression of ROR1 or ROR2 correlates with increased cancer metastatic potentials, and several anti-ROR therapies are currently in various stages of development (Rebagay et al., 2012). The etiological mechanisms of these mutations, however, remain largely uncharacterized. Thus, a greater understanding of ROR receptor function is important from both basic science and medical perspectives.

ROR receptors are type-I transmembrane proteins with a single-pass transmembrane (TM) helix linking extracellular and intracellular regions. The extracellular region of vertebrate ROR proteins contains an immunoglobulin (Ig) domain, a Frizzled-like cysteine rich domain (CRD) and a Kringle domain (Kr). The intracellular region includes a tyrosine kinase domain (Tk), a proline-rich domain (PRD), and two serine/threonine-rich domains (S/TRD 1 and 2) (Minami et al., 2010, Green et al., 2008). The specific requirement of these domains in WNT5A signaling remains controversial. Early genetic studies in *C. elegans* showed that only the CRD and the TM helix are essential for the function of the nematode ROR homolog Cam-1 in cell migration, which raised the possibility that Cam-1 may not act as a typical RTK and may instead regulate the spatial distribution of WNT ligands (Kim and Forrester, 2003). Experiments in vertebrate systems, however, largely suggest that ROR proteins act as bone fide signaling receptors and that this function requires other domains of ROR proteins, including the intracellular domains (DeChiara et al., 2000, Mikels et al., 2009). However, due to the historical lack of tractable assays to directly measure ROR activity, the precise requirement of vertebrate ROR proteins in noncanonical WNT5A signaling has not been systematically examined.

The CRD is of broader interest because it is not only conserved within the ROR family but also among other important receptor classes where the domain mediates ligand and/or co-factor binding through a signature hydrophobic groove or pocket (Bazan and de Sauvage, 2009). For instance, the CRD of the classical WNT receptor Frizzled interacts with the palmitoleate moiety of WNT ligands directly through this groove (Janda et al., 2012). Free fatty acids have also been observed to interact in the same fashion (Nile et al., 2017). Moreover, the CRD of the Hedgehog signal transducer and GPCR Smoothened (Smo) binds cholesterol through an analogous

hydrophobic pocket (Byrne et al., 2016). Because the CRD of ROR2 was previously implicated in WNT5A binding (Oishi et al., 2003), and shares a high degree of amino acid sequence similarity with the Frizzed CRD (Xu and Nusse, 1998, Saldanha et al., 1998), it is assumed that it possesses a similar hydrophobic groove via which it interacts with WNT5A. However, this hypothesis remains untested, as both the requirement of ROR2 CRD in WNT5A signaling and its atomic structure have not been determined.

In this study, we determined the crystal structure of the ROR2 CRD and Kr domains. Remarkably, we found that the two domains share an extended interface and that the ROR2 CRD lacks the characteristic hydrophobic groove/pocket for interacting with lipids. The latter observation suggests that the ROR2 CRD cannot mediate high-affinity interaction with the palmitoleate group of WNT5A. To further probe the requirement of the ROR2 CRD in WNT5A signaling, we developed a functional complementation assay in ROR1/ROR2 double knockout mouse embryonic fibroblasts (MEFs) and showed that the ROR2 CRD is required and minimally sufficient to mediate WNT5A-ROR signaling. Moreover, we used this assay paradigm to demonstrate that several Robinow patient mutations in the CRD and Kr domains compromise WNT5A-ROR signaling and offered structural insights into their possible underlying molecular defects. Lastly, using a highly specific monoclonal antibody that blocks Frizzled receptor activity, we established that the Frizzled family is required for the ability of the ROR2-CRD to mediate WNT5A signaling. Collectively, the study provides structural and functional insights into ROR2 function, and supports a model in which ROR2 functions through its CRD to promote Frizzled-dependent WNT5A signaling.

Results

The structure of the ROR2 CRD and Kr domains

To determine the structure of the ROR2 CRD, we expressed a range of constructs comprising the full-length human ROR2 extracellular region (Fig. 1A). Analysis of construct secretion revealed that deletion of the Kr domain severely impacted the yield of ROR2 constructs (Fig. S1A), and therefore the full extracellular region (ECD) and CRD-Kr were selected for large-scale expression and purification (Fig. S1B and C).

We determined a crystal structure of the ROR2 CRD-Kr tandem domain construct at a resolution of 2.7 Å via a platinum single-wavelength anomalous dispersion experiment coupled with molecular-replacement (MR-SAD) (Table S1, Fig. S1D-F; see experimental procedures for details). The CRD comprises 5 α-helices (α1-5) and a single β-sheet (strands β1 and β2), while the Kr domain presents a characteristic lack of secondary structure, displaying a single β-sheet (strands β3 and β4) (Fig .1B, left-hand panel). The CRD is stabilized by 5 disulfide bonds: one located between β1 and a loop extending from helix α2 (I), a second linking α2 and the loop preceding longest helix α1 (II), a third between helix α2 and the loop between helices α3/4 (III), a fourth between long loops following helices α2 and α3 (IV), and the fifth between helix α3 itself and the loop extending from α5 (V). The Kr domain is stabilized by 3 disulfide bonds, the first of which (VI) is formed between the very N-terminus and the C-terminus of the domain. Two additional disulfide bonds (VII and VIII) are found within the core of the Kr domain.

Overall, the CRD and Kr domains form an associated structural unit (Fig. 1B, right-hand panel). A contact interface is observed between the two domains and is dominated by van der Waals interactions, with a single hydrogen bond present (Fig. 1C). The domains share a small

121 interfacial area of 354 Å^2, with a reasonable shape complementarity score (0.7) (Lawrence and
122 Colman, 1993). Kr domains are generally observed to constitute protein-protein interfaces within
123 multi-domain proteins (Deguchi et al., 1997, Ultsch et al., 1998, Zebisch et al., 2016), suggesting
124 that the ROR2 Kr domain acts to stabilize the CRD (Fig. S1A).

125 The full-length ROR2 ECD is monomeric in solution at concentrations as high as 48 μM
126 (Fig. S1B and C), indicating that the CRD does not mediate dimerization as has been suggested
127 for other related Frizzled-type CRDs (Dann et al., 2001). The CRD-Kr structural unit arrangement
128 observed in the crystal structure is conserved in solution, confirmed by small-angle X-ray
129 scattering (SAXS) experiments (Fig. S2A-D), with the N-terminal Ig domain connected by a flexible
130 linker (Fig. S2C). Structurally, the ROR2 CRD is evolutionarily related to other Frizzled-type
131 'groove-containing' CRDs (Nachtergaele et al., 2013), such as MuSK and Fz8 (Fig. 1D and Table
132 S2) (Stiegler et al., 2009, Dann et al., 2001, Janda et al., 2012), as well as the cholesterol-binding
133 Hedgehog signal transducer Smo (Byrne et al., 2016). These are structurally distinct to the
134 'pocket-type' CRDs such as NPC1 and RFBP, which bury their physiological ligands in deep cavities
135 (Bazan and de Sauvage, 2009).

136

137 **Structural analysis of ROR2 CRD function**

138 The Frizzled-type CRDs from both Fz8 and Smo exhibit shallow hydrophobic grooves for the
139 binding of palmitoleate or cholesterol, respectively (Janda et al., 2012, Byrne et al., 2016) (Fig. 2).
140 One general characteristic differentiating this sub-family of CRDs from the 'pocket-type' sub-
141 family is that these grooves are structurally conserved when ligand-free (Fig. 2A and B), with
142 minimal structural rearrangements upon ligand binding (Dann et al., 2001, Janda et al., 2012,

Nachtergaele et al., 2013, Byrne et al., 2016). Despite structural conservation with other Frizzled-type receptors, the ROR2 CRD does not contain a visible hydrophobic groove pre-formed for ligand recognition (Fig. 2D). A structure-based sequence alignment shows that the ROR2 CRD has evolved an additional helical insertion (α5) relative to the FZD8 CRD (Fig. 2E). Structural superposition of the ROR2 CRD with the Fz8:Wnt-palmitoleate binary complex (Janda et al., 2012) shows that this helical insertion blocks exposure of any possible palmitoleate-binding groove (Fig. 2F and G). This observation is therefore incompatible with a direct binding event occurring between the ROR2 CRD and the WNT5A palmitoleate moiety, suggesting that the high affinity 'site 1' WNT5A interaction must occur either via a different site on the CRD or through a separate co-receptor(s), or require structural rearrangements as-yet not observed for groove-containing Fz-CRDs.

Functional requirement of the ROR2 CRD in WNT5A signaling

We next examined the requirement of the ROR2 CRD, as well as that of other ROR2 domains, in WNT5A signaling. We first developed a central rescue paradigm that allowed us to exogenously express various ROR2 mutant proteins in *ROR1/ROR2* double knockout (ROR DKO) mouse embryonic fibroblasts (MEFs) and assess their ability to restore WNT5A signaling (Fig. 3A). We isolated E12.5 primary MEFs from *ROR1/ROR2* double conditional mutant embryos for these experiments, as we previously showed that MEFs from this embryonic age are highly responsive to WNT5A-ROR signaling (Susman et al., 2017). To enable long-term genetic manipulations, we immortalized the MEFs (called iMEFs) via Cas9/CRISPR-mediated ablation of the *Tp53* gene (Dirac and Bernards, 2003). We then treated the iMEFs with 4-hydroxy-tamoxifen, which activates the

genetically encoded Cre-ER protein, to induce deletion of the *ROR1* and *ROR2* genes. To allow quantitative measurement of WNT5A-ROR signaling, we further engineered a GFP-Pdzrn3 degradation reporter construct into the iMEFs. We previously reported that activation of WNT5A-ROR signaling induces the proteasomal degradation of downstream effector protein Pdzrn3, and that this regulation could be recapitulated using the GFP-Pdzrn3 reporter in live cells via flow cytometry (Konopelski, 2021). Lastly, to compare the activities of wildtype (WT) ROR2 versus its mutant derivatives, we developed a lentivirus-based gene replacement strategy that allowed the expression of ROR2 "rescue" constructs at near-endogenous levels (See Materials and Methods for details). WNT5A dose-response analysis comparing ROR DKO reporter cells versus WT ROR2 rescued cells showed that re-expression of WT ROR2 promoted WNT5A signaling across all WNT5A doses tested (Fig. 3B). Notably, ROR DKO reporter cells without any ROR2 rescue still retained some basal WNT5A signaling activity, which remains dose-dependent with respect to WNT5A concentration (Fig. 3B). This observation indicates that, while ROR receptors play an impotent role in promoting WNT5A signaling, additional receptor(s) exist in these cells to transmit the WNT5A signal.

To systematically identify the domain(s) of ROR2 required for WNT5A signaling, we used our structural information to generate a series of ROR2 domain truncation mutants (Fig. 3C) and assessed their ability to restore WNT5A signaling in our iMEF signaling rescue assay (Fig. 3E). Immunoblotting confirmed that the mutant proteins were expressed at comparable levels as WT ROR2 (Fig. 3D). WNT5A stimulation experiments showed that ROR2 mutants lacking the CRD (ΔCRD and ΔCRD-Kr) failed to restore WNT5A-induced degradation of the GFP-Pdzrn3 reporter (Fig. 3E), establishing that the CRD is essential for WNT5A signaling. Surprisingly, all other

mutants in the series, including one lacking almost the entire intracellular region, still retain significant signaling capability, indicating that only the CRD is indispensible for the core function of ROR2 in promoting WNT5A signaling (Fig. 3E).

We next assessed the sufficiency of the ROR2 CRD in mediating WNT5A signaling. We engineered a chimeric construct (mini-ROR2) in which the isolated ROR2 CRD is fused to a generic transmembrane helix from CD45 (Chin et al., 2005), followed by a small, intracellular juxamembrane fragment (Fig. 3C). Expression of mini-ROR2 in the ROR DKO iMEF reporter cells was sufficient to partially rescue WNT5A signaling (Fig. 3E). This experiment, taken together with the truncation analysis, established that the ROR2-CRD is required and minimally sufficient to support the function of ROR2 in WNT5A signaling.

Co-requirement of Frizzled receptors in WNT5A-ROR signaling

Based on the observations that ROR DKO iMEFs still retain some signaling activity (Fig. 3B), and that ROR lacking the intracellular region can still function (Fig 3E), we postulated that ROR proteins cannot by themselves function as the signaling receptors for WNT5A; instead, they most likely facilitate the signaling function of another receptor(s). Members of the Frizzled family are likely candidates, as they are known to interact with WNT5A directly (Sato et al., 2010, Oishi et al., 2003) and have been implicated in aspects of WNT5A/ROR signaling (Grumolato et al., 2010, Oishi et al., 2003), and overexpression of Frizzleds can mimic the effect of WNT5A on Pdzrn3 degradation (Konopelski, 2021). To directly test the requirement of Frizzleds in WNT5A signaling, we treated our iMEF reporter cells with a synthetic monoclonal antibody, F2.A, that binds the CRD of many Frizzled family members and inhibits its ability to interact with WNTs (Pavlovic et

al., 2018). Indeed, this treatment completely blocked WNT5A-dependent degradation of the GFP-Pdzrn3 reporter in either ROR DKO iMEFs or ROR DKO iMEFs rescued with WT ROR2 (Fig. 3F). Thus, Frizzled receptors are required for WNT5A to signal the degradation of Pdzrn3, likely as part of a co-receptor complex with RORs (Fig. 3G).

Robinow syndrome mutations in the ROR2 CRD and Kr domains compromise WNT5A signaling

Of all the ROR2 domains, the CRD and Kr domains are most frequently mutated in Robinow syndrome patients (Tufan et al., 2005, Afzal et al., 2000, Tamhankar et al., 2014, Mehawej et al., 2012). Our structural and functional data suggest that these mutations would disrupt the function of ROR2 in WNT5A signaling. To test this hypothesis, we expressed and characterized five substitution mutations from Robinow patients that map to the CRD (C182Y, R184C, R189W, C223Y, R272C) and two that map to the Kr domain (G326A and R366W), using the ROR DKO iMEF rescue system. Western blot analysis showed that all seven mutant proteins were expressed at comparable levels as WT ROR2 (Fig. 4A). In WNT5A signaling assays, we found that three of the five CRD mutations (C182Y, R184C and C223Y) and both Kr mutations (G326A and R366W) exhibited significantly reduced signaling capabilities (Fig. 4B). These results indicate that disruption of ROR2 CRD/Kr function by these mutations is the likely molecular cause of Robinow syndrome.

Further insights into the pathogenic mechanisms of Robinow mutations were obtained from our structural analysis. C182Y and C223Y disrupt conserved cysteines in the CRD. Since our structure showed that all 10 cysteines in the CRD are involved in disulfide bond formation (Fig. 1B), these mutations likely cause Robinow syndrome by destabilizing the core structure of the

CRD (Fig. 4C, 4D and 4E). Two other mutations in the CRD (R184C and R272C) involve amino acid substitution to cysteines. Since both of these residues are solvent exposed (Fig. 4C, 4D and 4E), they may form cryptic intramolecular disulfide bonds that disrupt the protein fold, or alternatively form intermolecular disulfide bonds that cause inappropriate dimerization or oligomerization that results in protein aggregation. R189W and R272C did not show obvious functional deficit in our assay system. As the severity of Robinow syndrome can vary among individual patients and mutations, it is possible that more subtle defects are not detected by our system, or that they are involved in other aspects of ROR2 regulation beyond Pdzrn3 degradation.

Interestingly, the most detrimental mutations in the series (G326A and R366W) both map to the Kr domain at locations near the CRD-Kr interface (Fig. 4C and 4F). G326 in particular is situated near the linker between the CRD and Kr (Fig. 4C and 4C), and therefore, substitution at this position may open up the space between the two domains and expose hydrophobic residues to promote protein aggregation. Likewise, R366W may disrupt the overall fold of Kr, or disrupt the interface between the CRD and Kr to destabilize the CRD-Kr structural unit (Fig. 4C and 4C). Together, these functional and structural analyses provide crucial insights into the molecular mechanisms of Robinow pathogenesis.

Discussion

In this study, we used an integrated approach of structural biology, genetics and pharmacology to better understand the mechanism of WNT5A signal reception at the cell surface. We made several key observations that substantially advance our current understanding of WNT5A receptor function.

First, by solving the crystal structure of the ROR2 CRD, we made the surprising finding that this domain lacks the characteristic hydrophobic groove that binds the acyl moiety of WNTs and is thus incompatible with high affinity interaction with WNT ligands. Our experimental data agree with the modeling work by Janda and Garcia, who also predicted that the ROR2 CRD might not possess the hydrophobic groove to accommodate the lipid modification of WNTs (Janda and Garcia, 2015). This also agrees with the published crystal structure of MuSK, which is related to ROR2 and also lacks the hydrophobic groove in its CRD (Stiegler et al., 2009). The occlusion of the lipid/small molecule-binding site in ROR2 is unexpected and of general interst because this site was previously shown to play an important role not only for Wnt-Frizzled binding and Frizzled dimerization during canonical WNT signaling, but also for SMO function during Hedgehog signaling (Janda et al., 2012, Byrne et al., 2016, Nachtergaele et al., 2013, Nile et al., 2017). As there is clear evidence that the mammalian WNT5A is lipididated (Mikels and Nusse, 2006), our data raised the question of which co-receptor(s) in the pathway, if not ROR, is responsible for high-affinity WNT5A binding and signal transduction across the membrane. Though the exact identity of this co-receptor remains to be determined, our work points to the Frizzled receptor family, as blocking Frizzled function using a highly-specific and validated antibody blocked WNT5A signaling. We therefore favor a model in which WNT5A interacts with Frizzled with high affinity to transduce its signal across the plasma membrane, either by itself or in conjunction with another yet unidentified protein. However, this model does not rule out the possible presence of a low-affinity WNT5A binding site in the ROR2 CRD, analogous to the low affinity “site 2” observed in the WNT8-FZ8 complex (Janda et al., 2012). The ROR2 CRD could possibly sensitize WNT5A signaling by stabilizing the binding interaction between WNT5A and Frizzled via the

formation of a Frizzled:WNT:ROR2 super-complex (Fig. 3G). In this scenario, the WNT5A palmitoleate modification engages the Frizzled groove as previously described ('site 1')(Janda et al., 2012), whilst ROR2 binds at site 2 to recruit intracellular effectors of noncanonical WNT signaling. It is also possible that ROR2 acts by inducing an allosteric change in the structure of Frizzled to enhance Frizzled function or promotes Frizzled dimerization that in turn increases Frizzled's affinity for WNT5A (Carron et al., 2003, Nile et al., 2017).

Second, we observed that ROR2 mutants lacking the intracellular domain (ΔICD and mini-ROR2) can still support WNT5A signaling. This is inline with the idea that ROR2 itself is unlikely to be the signal-transmitting receptor for WNT5A. This idea is further supported by our observation that some residual signaling activity persists in cells lacking both ROR1 and ROR2 when stimulated with exogenously added WNT5A; we also show that this residual signaling activity is Frizzled-dependent. Collectively, these findings firmly established a co-requirement for both ROR and Frizzled activities in noncanonical WNT5A signal transduction. This model is also consistent with previous *in vivo* work showing that *ROR1/ROR2* double knockout mice phenocopy the characteristic tissue truncation phenotypes of *WNT5A* KO mice, and that human mutations in *WNT5A*, *ROR2* and *FZD2* can all cause Robinow syndrome with similar structural abnormalities (Nagasaki et al., 2018, White et al., 2018, Person et al., 2010, Afzal et al., 2000). Though several previous co-immunoprecipitation experiments have shown binding interactions between WNT5A and ROR2 (Oishi et al., 2003, Mikels and Nusse, 2006), between WNT5A and Frizzled family members (Sato et al., 2010), and between Frizzled and ROR proteins (Oishi et al., 2003), it remains unclear whether any of these biochemical interactions are direct. In light of our present work, it is crucial to further define these interactions quantitatively in future studies and to

297 understand their functions in the context of a co-receptor supercomplex. Nonetheless, our
298 results showing that ROR2 acts through its CRD to sensitize the function of Frizzleds or a Frizzled-
299 containing receptor complex during WNT5A-ROR signaling form the foundation for future
300 studies.

301 Lastly, our work provided new insights into the molecular mechanisms of Robinow
302 pathogenesis. Using the gene replacement strategy in iMEFs, we were able to directly assay the
303 function of Robinow syndrome mutant variants under highly physiological conditions. We found
304 that nearly all of the mutants tested exhibited defects in mediating WNT5A signaling, and that
305 mutating the cysteines required for disulfide bonds in the CRD is not tolerated. Furthermore, by
306 combining these functional data with our structural analysis, we can classify the mutations based
307 on their locations on the CRD-Kr structure and infer potential underlying mechanisms of signaling
308 perturbation. We envision that the experimental approach described in this study will serve as
309 an important model for interrogating other mutations in the pathway that cause Robinow
310 syndrome, brachydactyly type B and cancer metastasis, and more generally as a paradigm for
311 modeling genetic disorders.
312
313
314
315

316 **Supplementary Table 1. Data collection and refinement statistics for ROR2 CRD-Kr**
317

	ROR2 CRD-Kr (Native)	**ROR2 CRD-Kr (Pt-SAD)**	**ROR2-CRD-Kr (S-SAD)**
Data collection			
Beamline	DLS-I03	DLS-I03	DLS-I23
Space group	$P3_221$	$P3_121$	$P3_121$
Unit-cell parameters a, b, c (Å) α, β, γ (°)	 109.6, 109.6, 45.0 90.0, 90.0, 120.0	 106.1, 106.1, 42.2 90.0, 90.0, 120.0	 113.6, 113.6, 45.1 90.0, 90.0, 120.0
No. of crystals / data sets	1/1	2/2	1/1
Wavelength (Å)	0.9763	1.0500	1.7711
Resolution (Å)	54.80-2.70 (2.75-2.70)	53.00-3.00 (3.10-3.00)	56.80-2.95 (3.03-2.95)
No. of unique reflections	8699 (443)	5599 (397)	7171 (519)
Completeness (%)	99.4 (100.0)	99.9 (99.5)	98.6 (96.5)
Multiplicity	9.9 (8.7)	28.1 (24.3)	184.7 (38.7)
$\langle I/\sigma(I)\rangle$	16.3 (1.0)	23.5 (6.4)	25.0 (1.6)
R_{merge} (%)	7.8 (>100)	14.7 (59.6)	44.2 (>100)
R_{pim} (%)	2.6 (8.3)	3.0 (12.3)	3.2 (33.5)
$CC_{1/2}$	1.0 (0.5)	1.0 (0.8)	1.0 (0.9)
Refinement			
No. reflections (test set)	8688 (430)	-	
R_{work}/R_{free}	24.2 /25.6	-	
No. atoms			
Protein	1670	-	
Ligand	10	-	
Mean B factor (Å^2)			
Protein	112.0	-	
Ligand	137.1	-	
RMSD bond lengths (Å)	0.008	-	
RMSD bond angles (Å)	0.91	-	
Ramachandran plot (%)			
Favoured	96.1	-	
Allowed	3.4	-	
Outliers	0.5	-	

318

319 Data in parenthesis refer to highest resolution shell unless otherwise stated. RMSD: Root Mean
320 Square Derivative.
321

322 **Supplementary Table 2. Evolutionary analysis of CRD structures**.
323

Protein	Fz8-PAM (4F0A)[A]	Smo (5L7D)	Fz8 (1IJY)	sFRP3 (1IJX)	MuSK (3HKL)	NPC1 (3GKI)	RFBP (not in PDB)	FRα (4LRH)	JUNO (5EJN)	FRβ (4KMZ)
ROR2	1.19[B] 81[C] 39.62[D]	1.30 78 35.87	1.30 83 37.19	1.28 83 36.53	0.88 110 62.08	1.94 74 27.99	2.40 58 17.20	2.50 54 15.39	2.43 50 15.10	2.38 51 15.57
Fz8-PAM (4F0A)		1.00 83 43.64	0.16 117 102.54	0.42 106 79.01	1.30 78 38.33	2.17 61 21.36	2.54 40 13.35	2.76 44 12.16	2.51 44 13.31	2.44 43 14.14
Smo (5L7D)			1.09 84 43.18	1.04 80 44.60	1.26 78 40.84	2.32 54 19.01	2.68 46 11.24	2.62 46 13.73	2.64 44 12.47	2.49 48 15.65
Fz8 (1IJY)				0.45 108 78.07	1.35 76 36.13	2.14 62 22.27	2.50 45 15.00	2.66 43 13.41	2.38 45 15.40	2.53 43 14.34
sFRP3 (1IJX)					1.36 79 36.65	2.41 60 17.28	2.31 45 17.60	2.59 47 14.13	2.49 39 13.87	2.47 46 15.62
MuSK (3HKL)						2.14 67 22.48	2.25 55 20.03	2.30 55 15.14	2.16 53 19.21	2.13 53 23.24
NPC1 (3GKI)							1.73 82 35.46	1.95 89 31.57	1.74 81 36.37	1.74 90 30.58
RFBP (not in PDB)								0.68 160 104.06	0.85 138 80.30	0.66 157 105.39
FRα (4LRH)									0.42 161 125.21	0.16 194 176.05

JUNO (5EJN)										0.46 157 120.83

[A]PDB accession codes displayed in parenthesis; [B]RMSD values were calculated for equivalent Cα atom positions using the program SHP (Riffel et al., 2002; Stuart et al., 1979); [C]Number of equivalent Cα positions used in calculation of RMSD values with SHP; [D]Summed structural correlation (total probability) values calculated via SHP. The phylogenetic tree for CRDs analyzed (Fig. 1C) was assembled using PHYLIP (Felsenstein, 1989). These summed structural correlation values were used to construct a distance matrix. Fz8-PAM – Frizzled 8-palmitoleate complex (Janda et al., 2012), Smo – Smoothened (Byrne et al., 2016), Fz8 – Frizzled 8 (Dann et al., 2001), sFRP3 – secreted Frizzled-related protein 3 (Dann et al., 2001), MuSK – muscle-specific kinase (Stiegler et al., 2009), NPC1 – Niemann-Pick C1 protein (Kwon et al., 2009), RFBP – riboflavin-binding protein (Monaco, 1997), FRα – folate receptor α (Chen et al., 2013), FRβ – folate receptor β (Wibowo et al., 2013), JUNO – folate receptor δ (Han et al., 2016). Fz7 – Frizzled 7, Fz7-C24 – Frizzled 7-C24 fatty acid complex (Nile et al, 2017).

339 **Methods**

340 **Protein expression and purification.** Constructs of Human ROR2 (Genbank ID: 19743898)
341 comprising the ECD (residues 34-403), Ig-CRD (60-307), CRD-Kr (171-396) and CRD (171-307)
342 were cloned into the pHLsec vector in frame with a C-terminal His_6-tag (Aricescu et al., 2006).
343 ROR2 constructs were expressed by transient transfection in HEK293T cells with the addition of
344 glycosylation inhibitor kifunensine (Chang et al., 2007). Proteins were isolated from dialyzed
345 conditioned medium via immobilized metal-affinity chromatography and further purified via size
346 exclusion chromatography (SEC) in a buffer containing 10 mM HEPES pH 7.5, 150 mM NaCl.

347

348 **Crystallization and data collection.** Prior to crystallization trials, ROR2 CRD-Kr was concentrated
349 via ultrafiltration to a final concentration of 25 mg mL^{-1} and deglycosylated using a catalytic
350 quantities of endoglycosidase F1 (Chang et al., 2007) (0.2 µL/50 µL protein solution). Nanolitre-
351 scale crystallization trials were performed using a Cartesian Technologies robot (100 nL protein
352 plus 100 nL reservoir solution) in 96-well Greiner plates (Walter et al., 2005). ROR2 CRD-Kr
353 crystallized in 0.1 M HEPES pH 7.5, 1.5 M $LiSO_4$ at a temperature of 25°C. Diffraction data were
354 collected at a temperature of 100 K with crystals mounted within a liquid N_2 cryo-stream. Crystals
355 were treated with 20% (v/v) glycerol supplemented with reservoir solution and flash-cooled in
356 liquid N_2 prior to data collection. For Pt-SAD experiments, ROR2 CRD-Kr crystals were soaked in
357 0.1 M HEPES pH 7.5, 1.5 M $LiSO_4$ saturated with $KPtCl_6$ for 1 hour at 25°C prior to cryoprotection
358 and harvesting. Data were collected using the rotation method. Diffraction data were scaled and
359 merged using the XIA2 suite (Evans, 2006, Kabsch, 1988, Winter, 2010).

360

Structure solution. Initial phases for ROR2 CRD-Kr were obtained using Phenix Autosol with Pt-SAD data (Terwilliger et al., 2009). Four strong Pt sites were identified from substructure solution, and automated model building of the resultant electron density map was performed using the program *Buccaneer* (Cowtan, 2006). This produced an interpretable model for the CRD (residues 174-307), but phases were not of a high enough quality to properly trace the Kringle domain (residues 308-396). Subsequently, the CRD model generated was utilised as a molecular replacement search model in *Phaser* (McCoy et al., 2007) against higher resolution native data. This solution was fixed and a second search using a homology model for the Kringle domain (generated via Swiss-Model) was performed (Waterhouse et al., 2018). This strategy resulted higher scores in Phaser (LLG = 424, TFZ = 18.9) than searching for the CRD alone (LLG = 94, TFZ = 9.2), indicative of an improved solution. The model for the ROR2 CRD-Kr was manually built using COOT (Emsley and Cowtan, 2004) and refined to completion using AutoBUSTER (Smart et al., 2012).

Structure analysis. Stereochemistry was assessed using the MolProbity server (Davis et al., 2007). Superpositions were calculated using *Pymol* (Schrodinger, 2015), which was also used to create ray-traced protein structure images for figures. Residues involved in interactions were identified using both the PDBsum and Pisa servers (Krissinel and Henrick, 2007; Laskowski, 2001). The solvent accessible radius was set to 1.4 Å for the representation of all protein surfaces. Evolutionary structural analysis of CRDs was performed with *SHP* (Riffel et al., 2002; Stuart et al., 1979) and *PHYLIP* (Felsenstein, 1989) to assemble a phylogenetic tree. The structure-based

sequence alignment of ROR2 were generated using *UCSF Chimera* (Pettersen et al., 2004) and prepared for presentation using *ALINE* (Okabayashi et al., 1991).

SEC-MALS. 100 µL protein samples were injected onto an S200 10/30 column (GE Healthcare) equilibrated in a running buffer of 10 mM HEPES pH 7.5, 150 mM NaCl. For analysis of ROR2 oligomeric state, ROR2 ECD was injected at a concentration of 48 µM. A Wyatt Dawn HELEOS-II multi-angle light scattering (MALS) detector and Wyatt Optilab rEX refractive index monitor recorded both the refractive index and light scattering once separated via SEC. ASTRA software (Wyatt Technology) was utilized in data analysis.

Small-angle X-ray scattering (SAXS).

SAXS experiments were carried out on beamline B21, Diamond Light Source, UK at 25°C, over a momentum transfer (q) range of 0.01 $Å^{-1}$ < q < 0.45 $Å^{-1}$, where $q = 4\pi \sin(\theta)/\lambda$, and 2θ is the scattering angle. The ROR2 ECD was injected at onto an inline Shodex KW-402.5 SEC column at a concentration of 8 mg/mL, in a running buffer of 10 mM Tris pH 7.5, 150 mM NaCl, 1mM KNO_3. Data were collected with a beam energy of 12.4 keV using a Pilatus P3-2M detector. Data processing and reduction was performed using the program Scatter. Missing residues were added using Modeller (Eswar et al., 2003) and all-atom ensembles generated using Allosmod (Weinkam et al., 2012). In each case 50 independent ensembles of 100 models were created. Calculation and fitting of theoretical scattering curves to collected data was performed by FoXS (Schneidman-Duhovny et al., 2010). This procedure was automated via the use of Allosmod-FoXS (Guttman et al., 2013). Flexible models and were then generated using MultiFoXS (Schneidman-

Duhovny et al., 2016), as well as relative populations contributing to the overall scatter. This process produced 10000 conformations from the best-scoring model output from Allosmod, followed by scoring multi-state models fit to experimental scattering data as described above.

Mice

Ror1/2 double conditional KO mice were generated as previously described (Ho et al., 2012).

Cell lines

HEK293T (CRL-3216, ATCC, Manassas, VA) cells were purchased and not re-authenticated. All cell lines were cultured at 37 degree C and 5% CO2 in Dulbecco's 324 Modified Eagles Medium (MT15017CV, Corning) supplemented with 1x glutamine (25-005-CI, Corning), 1x 325 penicillin-streptomycin (30-002-CI, Corning) and 10% fetal bovine serum (16000069, Thermo Fisher Scientific).

For the derivation for iMEF reporter cells, primary *Ror1*$^{f/f}$*; Ror2*$^{f/f}$*; ER-cre* MEFs were isolated directly from E12.5 mouse embryos as described (Susman et al., 2017). Passage 1 or 2 cultures were then immortalized by electroporating with Cas9/CRISPR constructs targeting the *Tp53* genes using the Neon Transfection System (Thermo Fisher). Transformants were then serially passaged for 3-5 generations, or until cells from the untransfected control group have died off. For 4-hydroxytamoxifen (H7904; Sigma-Aldrich) treatments, cells were treated with 0.25 µM of 4-hydroxytamoxifen the first day and then 0.1 µM of 4-hydroxytamoxifen on the subsequent 3 days. The 4-hydroxyltamoxifen containing media were replenished daily. To introduce the GFP-Pdzrn3 degradation reporter, a PB (PiggyBac)-GFP-Pdzrn3 plasmid, along with

a Super PiggyBac Transposase-expressing plasmid, were electroporated into *Ror1$^{f/f}$; Ror2$^{f/f}$; ER-cre* iMEFs and then cultured for 7 days. GFP-positive cells were sorted (MoFlo Astrios Cell Sorter, Beckman Coulter, 488nm laser) to collect the weakly fluorescent (~lowest 1/3 on the FL scale) cells.

DNA constructs

Full-length mouse Ror2 was amplified from MEF cDNA and subsequently cloned into a modified pENTR-2B vector using FseI and AscI sites. Ror2 truncation mutants, Mini-Ror2 and Robinow syndrome mutants were generated through Gibson assembly. Open reading frames in pENTR-2B constructs were then transferred into pLEX_307 (a gift from David Root; Plasmid 41392, Addgene) or a modified pLEX_307 lentiviral vector (short EF1 pLEX_307) in which the intron in the EF1 promoter has been moved, using the Gateway LR Clonase II enzyme mix (11791020, Thermo Fisher). The open-reading frames in all constructs were verified by Sanger sequencing.

Lentiviral protein overexpression

Lentiviruses were packaged and produced in HEK293T cells by co-transfection of the lentiviral vectors with the following packaging plasmids: pRSV-REV, pMD-2-G and pMD-Lg1-pRRE (gifts from Thomas Vierbuchen). 0.1ml or 0.45ml of the viral supernatants was used to infect *Ror1$^{f/f}$; Ror2$^{f/f}$; ER-cre* iMEFs iMEFs seeded at 50% confluency in 12-well plates (per well) for ~16 hrs. Following removal of the virus-containing media, cells were cultured for 24 hrs. Infected cells were then selected with puromycin (0.002 mg/ml) for 3 days. Cells from the viral titer that killed

a large proportion of cells (60–90%) were expanded and used for FACS; this ensured that the multiplicity of infection (MOI) is ~1 for all cell lines used in the experiments.

Antibodies

Antibodies against Ror1, Ror2, and Kif26b were described previously (Ho et al., 2012, Susman et al., 2017). The following antibodies were purchased: rabbit anti-Dvl2 (3216, Cell Signaling); mouse anti-α-tubulin (clone 371 DM1A, ab7291, Abcam); mouse anti-Flag (M2, F1804, Sigma-Aldrich). Antibodies against Pdzrn3 were described previously (Konopelski, 2021).

Western blotting

Protein lysates for SDS-PAGE and western blotting were prepared in 1x - 2x Laemmli sample buffer or LDS sample buffer (NP0007, Life Technologies). All protein lysates were heated at 95C for 10min before SDS-PAGE and western blotting. Quantitative western blotting was performed using the Sapphire gel Imager (Azure BioSystems) according to the manufacturer's instructions. Non-saturated protein bands were quantified by using Sapphire gel Imager with the gamma level set at 1.

Recombinant proteins and inhibitors

The following recombinant proteins and drugs were purchased: human/mouse WNT5A (654-WN-010, R&D Systems); Wnt-C59 (C7641-2s; Cellagen Technology); 4-hydroxytamoxifen (H7904; Sigma-Aldrich). The F2.A anti-Frizzled antibody was previously described (Pavlovic et al., 2018)

469 **Flow cytometry-based WNT5A signaling assay**

470 Immortalized MEF cells expressing the GFP-Pdzrn3 reporter were plated at a density of
471 0.08 million/well in a poly-D-lysine-coated 48-well plate. 12 hr after plating, the cells were
472 incubated with 10 nM Wnt-C59 and allowed to reach confluency. 72 hr after plating, cells were
473 stimulated with either WNT5A proteins or an equivalent volume of the control buffer (PBS with
474 0.1% BSA and 0.5% (w/v) CHAPS) in the presence of 10 nM Wnt-C59 for 6 hr. Cells were then
475 harvested, resuspended in PBS + 0.5% FBS and analyzed using a flow cytometer (FACScan with a
476 500 nm laser, Becton Dickinson). Raw data were acquired with CellQuest (Becton Dickinson) and
477 processed in FlowJoX (FLOWJO). Processing entailed gating out dead cells, calculation of median
478 fluorescence, percent change of medians, and overlay of histograms. For WNT5A dose-response
479 experiments (Fig. 3B and 3F), cells were treated with the indicated concentrations of WNT5A for
480 16 hr. For mutant analysis (Fig. 3E and 4B), cells were treated with 200nM WNT5A for 6 hr. For
481 anti-Frizzled antibody treatment, the F2.A antibody was added to the cells 2 hrs before the start
482 of WNT5A stimulation and maintained throughout the experiment.

483

484 **Acknowledgements**

485 We thank members of the Siebold and Ho labs for their input and discussions. We thank the staff
486 of Diamond Light Source UK beamlines I03, I23 and B21 for assistance (MX14744 and MX19946),
487 and K. El Omari, T. Walter, K. Harlos and D. Staunton for technical support. This work was
488 supported by a National Institutes of Health grant 1R35GM119574 to Hsin-Yi Henry Ho, and
489 Cancer Research UK (C20724/A26752) to C.S. S.C.G. was supported by a Wellcome Trust-funded

DPhil studentship (099675/Z/12/Z). Additional support from the Wellcome Trust Core Award Grant Number 203141/Z/16/Z is acknowledged.

References

AFZAL, A. R., RAJAB, A., FENSKE, C. D., OLDRIDGE, M., ELANKO, N., TERNES-PEREIRA, E., TUYSUZ, B., MURDAY, V. A., PATTON, M. A., WILKIE, A. O. & JEFFERY, S. 2000. Recessive Robinow syndrome, allelic to dominant brachydactyly type B, is caused by mutation of ROR2. *Nat Genet,* 25**,** 419-22.

BAZAN, J. F. & DE SAUVAGE, F. J. 2009. Structural ties between cholesterol transport and morphogen signaling. *Cell,* 138**,** 1055-6.

BUNN, K. J., DANIEL, P., ROSKEN, H. S., O'NEILL, A. C., CAMERON-CHRISTIE, S. R., MORGAN, T., BRUNNER, H. G., LAI, A., KUNST, H. P., MARKIE, D. M. & ROBERTSON, S. P. 2015. Mutations in DVL1 cause an osteosclerotic form of Robinow syndrome. *Am J Hum Genet,* 96**,** 623-30.

BYRNE, E. F. X., SIRCAR, R., MILLER, P. S., HEDGER, G., LUCHETTI, G., NACHTERGAELE, S., TULLY, M. D., MYDOCK-MCGRANE, L., COVEY, D. F., RAMBO, R. P., SANSOM, M. S. P., NEWSTEAD, S., ROHATGI, R. & SIEBOLD, C. 2016. Structural basis of Smoothened regulation by its extracellular domains. *Nature,* 535**,** 517-522.

CARRON, C., PASCAL, A., DJIANE, A., BOUCAUT, J. C., SHI, D. L. & UMBHAUER, M. 2003. Frizzled receptor dimerization is sufficient to activate the Wnt/beta-catenin pathway. *J Cell Sci,* 116**,** 2541-50.

CHIN, C. N., SACHS, J. N. & ENGELMAN, D. M. 2005. Transmembrane homodimerization of receptor-like protein tyrosine phosphatases. *FEBS Lett,* 579**,** 3855-8.

DANN, C. E., HSIEH, J. C., RATTNER, A., SHARMA, D., NATHANS, J. & LEAHY, D. J. 2001. Insights into Wnt binding and signalling from the structures of two Frizzled cysteine-rich domains. *Nature,* 412**,** 86-90.

DECHIARA, T. M., KIMBLE, R. B., POUEYMIROU, W. T., ROJAS, J., MASIAKOWSKI, P., VALENZUELA, D. M. & YANCOPOULOS, G. D. 2000. Ror2, encoding a receptor-like tyrosine kinase, is required for cartilage and growth plate development. *Nat Genet,* 24**,** 271-4.

DEGUCHI, H., TAKEYA, H., GABAZZA, E. C., NISHIOKA, J. & SUZUKI, K. 1997. Prothrombin kringle 1 domain interacts with factor Va during the assembly of prothrombinase complex. *Biochem J,* 321 (Pt 3)**,** 729-35.

DIRAC, A. M. & BERNARDS, R. 2003. Reversal of senescence in mouse fibroblasts through lentiviral suppression of p53. *J Biol Chem,* 278**,** 11731-4.

ESWAR, N., JOHN, B., MIRKOVIC, N., FISER, A., ILYIN, V. A., PIEPER, U., STUART, A. C., MARTI-RENOM, M. A., MADHUSUDHAN, M. S., YERKOVICH, B. & SALI, A. 2003. Tools for comparative protein structure modeling and analysis. *Nucleic Acids Res,* 31**,** 3375-80.

EVANS, P. 2006. Scaling and assessment of data quality. *Acta Crystallogr D Biol Crystallogr,* 62**,** 72-82.

GREEN, J. L., KUNTZ, S. G. & STERNBERG, P. W. 2008. Ror receptor tyrosine kinases: orphans no more. *Trends Cell Biol,* 18**,** 536-44.

GRUMOLATO, L., LIU, G., MONG, P., MUDBHARY, R., BISWAS, R., ARROYAVE, R., VIJAYAKUMAR, S., ECONOMIDES, A. N. & AARONSON, S. A. 2010. Canonical and noncanonical Wnts use a common mechanism to activate completely unrelated coreceptors. *Genes Dev,* 24**,** 2517-30.

GUTTMAN, M., WEINKAM, P., SALI, A. & LEE, K. K. 2013. All-atom ensemble modeling to analyze small-angle x-ray scattering of glycosylated proteins. *Structure,* 21**,** 321-31.

HO, H. Y., SUSMAN, M. W., BIKOFF, J. B., RYU, Y. K., JONAS, A. M., HU, L., KURUVILLA, R. & GREENBERG, M. E. 2012. Wnt5a-Ror-Dishevelled signaling constitutes a core developmental pathway that controls tissue morphogenesis. *Proc Natl Acad Sci U S A,* 109**,** 4044-51.

JANDA, C. Y. & GARCIA, K. C. 2015. Wnt acylation and its functional implication in Wnt signalling regulation. *Biochem Soc Trans,* 43**,** 211-6.

JANDA, C. Y., WAGHRAY, D., LEVIN, A. M., THOMAS, C. & GARCIA, K. C. 2012. Structural basis of Wnt recognition by Frizzled. *Science,* 337**,** 59-64.

KABSCH, W. 1988. Automatic indexing of rotation diffraction patterns. *J. Appl. Cryst.,* 21**,** 67-72.

KIM, C. & FORRESTER, W. C. 2003. Functional analysis of the domains of the C elegans Ror receptor tyrosine kinase CAM-1. *Dev Biol,* 264**,** 376-90.

KONOPELSKI, S. E., SUSMAN MW, KUNZ R, TAN J, COHEN MD, OKADA K, LAMB H, CHOI SC, KARUNA EP, SCALES MK, GYGI SP, GREENBERG ME, HO HH. 2021. Proteomic analysis identifies the E3 ubiquitin ligase Pdzrn3 as a regulatory target of Wnt5a-Ror signaling. *Proc Natl Acad Sci U S A,* 118**,** e2104944118.

MEHAWEJ, C., CHOUERY, E., MAALOUF, D., BAUJAT, G., LE MERRER, M., CORMIER-DAIRE, V. & MEGARBANE, A. 2012. Identification of a novel causative mutation in the ROR2 gene in a Lebanese family with a mild form of recessive Robinow syndrome. *Eur J Med Genet,* 55**,** 103-8.

MIKELS, A., MINAMI, Y. & NUSSE, R. 2009. Ror2 receptor requires tyrosine kinase activity to mediate Wnt5A signaling. *J Biol Chem,* 284**,** 30167-76.

MIKELS, A. J. & NUSSE, R. 2006. Purified Wnt5a protein activates or inhibits beta-catenin-TCF signaling depending on receptor context. *PLoS Biol,* 4**,** e115.

MINAMI, Y., OISHI, I., ENDO, M. & NISHITA, M. 2010. Ror-family receptor tyrosine kinases in noncanonical Wnt signaling: their implications in developmental morphogenesis and human diseases. *Dev Dyn,* 239**,** 1-15.

MOON, R. T., CAMPBELL, R. M., CHRISTIAN, J. L., MCGREW, L. L., SHIH, J. & FRASER, S. 1993. Xwnt-5A: a maternal Wnt that affects morphogenetic movements after overexpression in embryos of Xenopus laevis. *Development,* 119**,** 97-111.

NACHTERGAELE, S., WHALEN, D. M., MYDOCK, L. K., ZHAO, Z., MALINAUSKAS, T., KRISHNAN, K., INGHAM, P. W., COVEY, D. F., SIEBOLD, C. & ROHATGI, R. 2013. Structure and function of the Smoothened extracellular domain in vertebrate Hedgehog signaling. *Elife,* 2**,** e01340.

NAGASAKI, K., NISHIMURA, G., KIKUCHI, T., NYUZUKI, H., SASAKI, S., OGAWA, Y. & SAITOH, A. 2018. Nonsense mutations in FZD2 cause autosomal-dominant omodysplasia: Robinow syndrome-like phenotypes. *Am J Med Genet A,* 176**,** 739-742.

NILE, A. H., MUKUND, S., STANGER, K., WANG, W. & HANNOUSH, R. N. 2017. Unsaturated fatty acyl recognition by Frizzled receptors mediates dimerization upon Wnt ligand binding. *Proc Natl Acad Sci U S A,* 114**,** 4147-4152.

OISHI, I., SUZUKI, H., ONISHI, N., TAKADA, R., KANI, S., OHKAWARA, B., KOSHIDA, I., SUZUKI, K., YAMADA, G., SCHWABE, G. C., MUNDLOS, S., SHIBUYA, H., TAKADA, S. & MINAMI, Y. 2003. The receptor tyrosine kinase Ror2 is involved in non-canonical Wnt5a/JNK signalling pathway. *Genes Cells,* 8**,** 645-54.

OKABAYASHI, K., NAKAGAWA, Y., HAYASUKE, N., OHI, H., MIURA, M., ISHIDA, Y., SHIMIZU, M., MURAKAMI, K., HIRABAYASHI, K., MINAMINO, H. & ET AL. 1991. Secretory expression of the human serum albumin gene in the yeast, Saccharomyces cerevisiae. *J Biochem,* 110**,** 103-10.

OLDRIDGE, M., FORTUNA, A. M., MARINGA, M., PROPPING, P., MANSOUR, S., POLLITT, C., DECHIARA, T. M., KIMBLE, R. B., VALENZUELA, D. M., YANCOPOULOS, G. D. & WILKIE, A. O. 2000. Dominant mutations in ROR2, encoding an orphan receptor tyrosine kinase, cause brachydactyly type B. *Nat Genet,* 24**,** 275-8.

PAVLOVIC, Z., ADAMS, J. J., BLAZER, L. L., GAKHAL, A. K., JARVIK, N., STEINHART, Z., ROBITAILLE, M., MASCALL, K., PAN, J., ANGERS, S., MOFFAT, J. & SIDHU, S. S. 2018. A synthetic anti-Frizzled antibody engineered for broadened specificity exhibits enhanced anti-tumor properties. *MAbs,* 10**,** 1157-1167.

PERSON, A. D., BEIRAGHI, S., SIEBEN, C. M., HERMANSON, S., NEUMANN, A. N., ROBU, M. E., SCHLEIFFARTH, J. R., BILLINGTON, C. J., JR., VAN BOKHOVEN, H., HOOGEBOOM, J. M., MAZZEU, J. F., PETRYK, A., SCHIMMENTI, L. A., BRUNNER, H. G., EKKER, S. C. & LOHR, J. L. 2010. WNT5A mutations in patients with autosomal dominant Robinow syndrome. *Dev Dyn,* 239**,** 327-37.

REBAGAY, G., YAN, S., LIU, C. & CHEUNG, N. K. 2012. ROR1 and ROR2 in Human Malignancies: Potentials for Targeted Therapy. *Front Oncol,* 2**,** 34.

SALDANHA, J., SINGH, J. & MAHADEVAN, D. 1998. Identification of a Frizzled-like cysteine rich domain in the extracellular region of developmental receptor tyrosine kinases. *Protein Sci,* 7**,** 1632-5.

SATO, A., YAMAMOTO, H., SAKANE, H., KOYAMA, H. & KIKUCHI, A. 2010. Wnt5a regulates distinct signalling pathways by binding to Frizzled2. *EMBO J,* 29**,** 41-54.

SCHNEIDMAN-DUHOVNY, D., HAMMEL, M. & SALI, A. 2010. FoXS: a web server for rapid computation and fitting of SAXS profiles. *Nucleic Acids Res,* 38**,** W540-4.

SCHNEIDMAN-DUHOVNY, D., HAMMEL, M., TAINER, J. A. & SALI, A. 2016. FoXS, FoXSDock and MultiFoXS: Single-state and multi-state structural modeling of proteins and their complexes based on SAXS profiles. *Nucleic Acids Res,* 44**,** W424-9.

SCHWABE, G. C., TINSCHERT, S., BUSCHOW, C., MEINECKE, P., WOLFF, G., GILLESSEN-KAESBACH, G., OLDRIDGE, M., WILKIE, A. O., KOMEC, R. & MUNDLOS, S. 2000. Distinct mutations in the receptor tyrosine kinase gene ROR2 cause brachydactyly type B. *Am J Hum Genet,* 67**,** 822-31.

STIEGLER, A. L., BURDEN, S. J. & HUBBARD, S. R. 2009. Crystal structure of the frizzled-like cysteine-rich domain of the receptor tyrosine kinase MuSK. *J Mol Biol,* 393**,** 1-9.

SUSMAN, M. W., KARUNA, E. P., KUNZ, R. C., GUJRAL, T. S., CANTU, A. V., CHOI, S. S., JONG, B. Y., OKADA, K., SCALES, M. K., HUM, J., HU, L. S., KIRSCHNER, M. W., NISHINAKAMURA, R.,

YAMADA, S., LAIRD, D. J., JAO, L. E., GYGI, S. P., GREENBERG, M. E. & HO, H. H. 2017. Kinesin superfamily protein Kif26b links Wnt5a-Ror signaling to the control of cell and tissue behaviors in vertebrates. *Elife,* 6.

TAMHANKAR, P. M., VASUDEVAN, L., KONDURKAR, S., YASHASWINI, K., AGARWALLA, S. K., NAIR, M., RAMKUMAR, T. V., CHAUBAL, N. & CHENNURI, V. S. 2014. Identification of novel ROR2 gene mutations in Indian children with Robinow syndrome. *J Clin Res Pediatr Endocrinol,* 6**,** 79-83.

TUFAN, F., CEFLE, K., TURKMEN, S., TURKMEN, A., ZORBA, U., DURSUN, M., OZTURK, S., PALANDUZ, S., ECDER, T., MUNDLOS, S. & HORN, D. 2005. Clinical and molecular characterization of two adults with autosomal recessive Robinow syndrome. *Am J Med Genet A,* 136**,** 185-9.

ULTSCH, M., LOKKER, N. A., GODOWSKI, P. J. & DE VOS, A. M. 1998. Crystal structure of the NK1 fragment of human hepatocyte growth factor at 2.0 A resolution. *Structure,* 6**,** 1383-93.

VAN BOKHOVEN, H., CELLI, J., KAYSERILI, H., VAN BEUSEKOM, E., BALCI, S., BRUSSEL, W., SKOVBY, F., KERR, B., PERCIN, E. F., AKARSU, N. & BRUNNER, H. G. 2000. Mutation of the gene encoding the ROR2 tyrosine kinase causes autosomal recessive Robinow syndrome. *Nat Genet,* 25**,** 423-6.

VEEMAN, M. T., AXELROD, J. D. & MOON, R. T. 2003. A second canon. Functions and mechanisms of beta-catenin-independent Wnt signaling. *Dev Cell,* 5**,** 367-77.

WATERHOUSE, A., BERTONI, M., BIENERT, S., STUDER, G., TAURIELLO, G., GUMIENNY, R., HEER, F. T., DE BEER, T. A. P., REMPFER, C., BORDOLI, L., LEPORE, R. & SCHWEDE, T. 2018. SWISS-MODEL: homology modelling of protein structures and complexes. *Nucleic Acids Res,* 46**,** W296-W303.

WEINKAM, P., PONS, J. & SALI, A. 2012. Structure-based model of allostery predicts coupling between distant sites. *Proc Natl Acad Sci U S A,* 109**,** 4875-80.

WHITE, J., MAZZEU, J. F., HOISCHEN, A., JHANGIANI, S. N., GAMBIN, T., ALCINO, M. C., PENNEY, S., SARAIVA, J. M., HOVE, H., SKOVBY, F., KAYSERILI, H., ESTRELLA, E., VULTO-VAN SILFHOUT, A. T., STEEHOUWER, M., MUZNY, D. M., SUTTON, V. R., GIBBS, R. A., BAYLOR-HOPKINS CENTER FOR MENDELIAN, G., LUPSKI, J. R., BRUNNER, H. G., VAN BON, B. W. & CARVALHO, C. M. 2015. DVL1 frameshift mutations clustering in the penultimate exon cause autosomal-dominant Robinow syndrome. *Am J Hum Genet,* 96**,** 612-22.

WHITE, J. J., MAZZEU, J. F., COBAN-AKDEMIR, Z., BAYRAM, Y., BAHRAMBEIGI, V., HOISCHEN, A., VAN BON, B. W. M., GEZDIRICI, A., GULEC, E. Y., RAMOND, F., TOURAINE, R., THEVENON, J., SHINAWI, M., BEAVER, E., HEELEY, J., HOOVER-FONG, J., DURMAZ, C. D., KARABULUT, H. G., MARZIOGLU-OZDEMIR, E., CAYIR, A., DUZ, M. B., SEVEN, M., PRICE, S., FERREIRA, B. M., VIANNA-MORGANTE, A. M., ELLARD, S., PARRISH, A., STALS, K., FLORES-DABOUB, J., JHANGIANI, S. N., GIBBS, R. A., BAYLOR-HOPKINS CENTER FOR MENDELIAN, G., BRUNNER, H. G., SUTTON, V. R., LUPSKI, J. R. & CARVALHO, C. M. B. 2018. WNT Signaling Perturbations Underlie the Genetic Heterogeneity of Robinow Syndrome. *Am J Hum Genet,* 102**,** 27-43.

WHITE, J. J., MAZZEU, J. F., HOISCHEN, A., BAYRAM, Y., WITHERS, M., GEZDIRICI, A., KIMONIS, V., STEEHOUWER, M., JHANGIANI, S. N., MUZNY, D. M., GIBBS, R. A., BAYLOR-HOPKINS CENTER FOR MENDELIAN, G., VAN BON, B. W. M., SUTTON, V. R., LUPSKI, J. R., BRUNNER,

H. G. & CARVALHO, C. M. B. 2016. DVL3 Alleles Resulting in a -1 Frameshift of the Last Exon Mediate Autosomal-Dominant Robinow Syndrome. *Am J Hum Genet,* 98**,** 553-561.

WINTER, G. 2010. xia2: an expert system for macromolecular crystallography data reduction. *J. Appl. Cryst.,* 43**,** 186-190.

XU, Y. K. & NUSSE, R. 1998. The Frizzled CRD domain is conserved in diverse proteins including several receptor tyrosine kinases. *Curr Biol,* 8**,** R405-6.

ZEBISCH, M., JACKSON, V. A., ZHAO, Y. & JONES, E. Y. 2016. Structure of the Dual-Mode Wnt Regulator Kremen1 and Insight into Ternary Complex Formation with LRP6 and Dickkopf. *Structure,* 24**,** 1599-605.

Figure Legends

Figure 1. Structure of the ROR2 CRD and Kringle domains. **A)** Domain layout of ROR2 and constructs used in this study. **B)** Cartoon representation of the ROR2 CRD-Kr structural unit coloured in a rainbow representation (N terminus: blue, C terminus:red), with secondary structural elements indicated and disulfide bonds numbered using Roman numerals. The right panel shows a 2-domain representation of ROR2, with the CRD in salmon and the Kringle domain in blue. **C)** Close-up view on the ROR2 CRD-Kr interface rotated 90^{o} relative to **B**. Interface residues are shown in stick representation and colour-coded as in B, right panel. A single hydrogen bond is displayed as a dashed line. **D)** Structural phylogenetic analysis of CRDs, adapted from (Nachtergaele et al., 2013) to include ROR2.

Figure 2. Comparison of the ROR2 CRD to other Fz-type CRDs. **A-D)** CRDs are shown as surface representation and coloured according hydrophobicity (green: hydrophobic to white:hydrophilic). Displayed structures: **A)** Fz8-PAM (palmitoleate) complex (PDB 4F0A) (Janda et al., 2012), **B)** Fz-apo (PDB 1IJY) (Dann et al., 2001), **C)** Smoothened-CLR (cholesterol) complex (PDB 5L7D) (Byrne et al., 2016) and **D)** ROR2 (from this study). **E-F)** Structural comparison of the

CRDs from ROR2 (salmon) and Fz8 (green). A structure-based sequence alignment (**E**) corresponding structural superposition (**F)** are shown. Regions of Wnt8 observed to interact with Fz8 are displayed in purple. **G)** Analysis of the "Site 1"-interacting region. The Wnt8 lipid thumb is shown in purple, with the covalently-attached palmitoleate moiety (PAM) as white sticks. The lipid-binding groove of Fz8 is displayed as a transparent green surface. A dashed arrow indicates the required movement of ROR2 helix α5 in order to prevent a steric clash with the Wnt8 lipid thumb.

Figure S1. ROR2 purification, characterization and structure solution. **A)** Western blot analysis of the secretion of soluble ROR2 constructs from HEK293T cells. Deletion of the Kringle domain impairs secretion. **B)** SEC-MALS analysis of the ROR2 ECD at 2 mg mL^{-1} (48 µM). The ROR2 ECD elutes as a monomeric species with a molecular weight of 45.4 kDa. **C)** Purity assessment by SDS-PAGE of ROR2 ECD construct purified via IMAC and SEC. **D)** Structure solution of ROR2 Fz-Kr using MR-SAD. Pt-soaked crystals enabled the determination of a model for the Fz-CRD using *Phenix Autosol* (yellow, left). The Kringle domain could not be built without an MR search using an ensemble of homology models generated using *Rosetta*. The final structure was refined using *AutoBUSTER* (salmon/blue, right). **E)** Identification of sulfur sites in ROR2 Fz-Kr using long-wavelength data collection at I23. A total of 8 disulfide bonds (I-VIII) could be resolved, as well as 4 methionine side chains (Met-1 to Met-4) and 2 sulphate ions. **F)** Disulfide bond VI is in a flexible region between the two domains, but is accounted for in the anomalous map. Anomalous difference density is contoured at 3σ (yellow) and 2Fo-Fc density at 1σ (blue).

Figure S2. SAXS solution structure of the ROR2 ECD. A) Experimental scattering curve (black) and calculated scattering from models (blue), shown to a maximum momentum transfer of 0.35 $Å^{-1}$. A fitting residual between the experimental and calculated scattering patterns is displayed. **B)** Full-length models of the ROR2 ECD and their relative populations contributing to the model scattering curve, as calculated by Multi-FOXS. **C)** Experimental (black) and calculated (blue) Guinier region. The shaded area indicates the region used for R_g analysis. The calculated radius of gyration ($R_{g)}$ and molecular weight derived from the volume of correlation metric V_c (MW_{VC}) are displayed. **D)** Normalised pair distance distribution (P(r)) function and derived maximum intra-particle distance distribution function (D_{max}).

Figure 3. Requirement of the ROR2 CRD and Frizzleds in WNT5A signaling

A) Workflow of the ROR2 central rescue paradigm. Primary MEF cultures generated from E12.5 *ROR1$^{f/f}$; ROR2$^{f/f}$; Cre-ER* mouse embryos were immortalized by CRISPR/Cas9-mediated deletion of the *Tp53* gene. A WNT5A-ROR signaling reporter (GFP-Pdzrn3) was stably inserted in the immortalized MEFs (iMEFs) via lentiviral transduction. *ROR1/ROR2* conditional mutant iMEFs were then treated with 4-OHT to activate the Cre-ER recombinase and delete the *ROR1* and *ROR2* genes. To test the function of mutant ROR2 variants, WT or mutant ROR2 proteins were re-expressed in *ROR1/ROR2* double KO (ROR DKO) iMEFs via lentiviral transduction. **B)** Dose-response curves showing WNT5A-ROR signaling activity, as assayed by GFP-Pdzrn3 degradation, as a function of WNT5A concentration in ROR DKO iMEFs or ROR DKO iMEFs re-expressing WT ROR2. Each datapoint was calculated from the median fluorescence (after WNT5A stimulation – before WNT5A stimulation/before WNT5A stimulation) of the GFP-Pdzrn3 reporter from 20,000

– 30,000 cells. **C)** Schematic of ROR2 truncation mutants and the mini-ROR2 construct. **D)** Western blot showing expression of the endogenous ROR2 in the ROR double conditional KO iMEFs (Lane 1), the abolition of ROR2 expression in ROR DKO iMEFs (Lane 2), the re-expression of WT (Lane 3) and mutant ROR2 variants (Lanes 4-9). The WT or mutant ROR2 bands are marked with asterisks for clarity. Tubulin was used as the loading control. **E)** Quantification of the effects of ROR2 mutant variants in rescuing WNT5A-ROR signaling, as assayed by GFP-Pdzrn3 degradation. Error bars represent ± SEM calculated from three technical replicates. t-test (unpaired) was performed to determine statistical significance for mutants vs. WT ROR2 rescue. **F)** Effects of the anti-Frizzled antibody F2.A on WNT5A signaling, as assayed by GFP-Pdzrn3 degradation in ROR DKO iMEFs or ROR DKO iMEFs re-expressing WT ROR2, over a range of WNT5A doses. Each datapoint was calculated from the median fluorescence (after WNT5A stimulation – before WNT5A stimulation/before WNT5A stimulation) of the GFP-Pdzrn3 reporter from 20,000 – 30,000 cells. **G)** Model of ROR2 CRD and Frizzled action in WNT5A-ROR signaling.

Figure 4. Analysis of Robinow syndrome mutations in the ROR2 CRD and Kr

A) Western blot showing expression of WT ROR2 and Robinow syndrome ROR2 mutants in the ROR DKO iMEF reporter cells. **B)** Quantification of the effects of Robinow syndrome ROR2 mutants in rescuing WNT5A-ROR signaling, as assayed by GFP-Pdzrn3 degradation. Error bars represent ± SEM calculated from three technical replicates. t-test (unpaired) was performed to determine statistical significance for mutants vs. WT ROR2 rescue. **C)** Structure of the ROR2 CRD-Kr tandem domains showing the location of the Robinow syndrome mutations. **D)** Close-

751 up view of C223 and R272. **E)** Close-up view of C182, R184 and R189. **F)** Close-up view of G326

752 and R366.

Figure 1

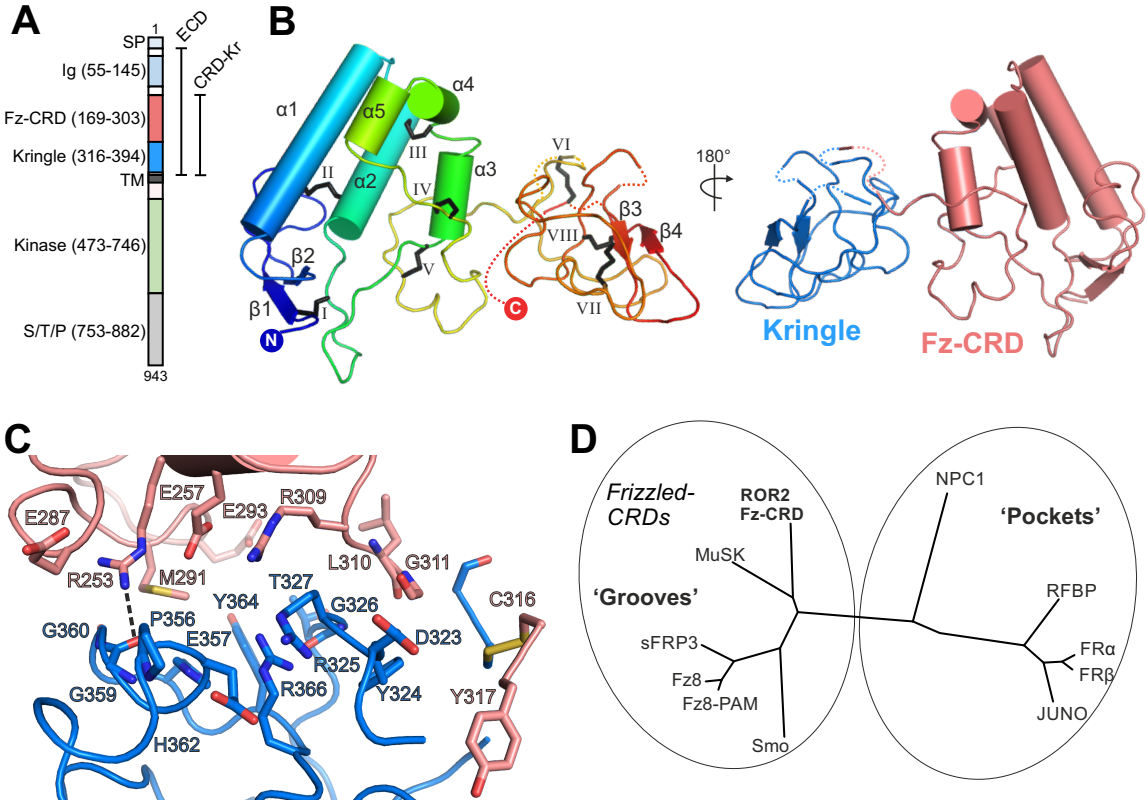

Figure S1

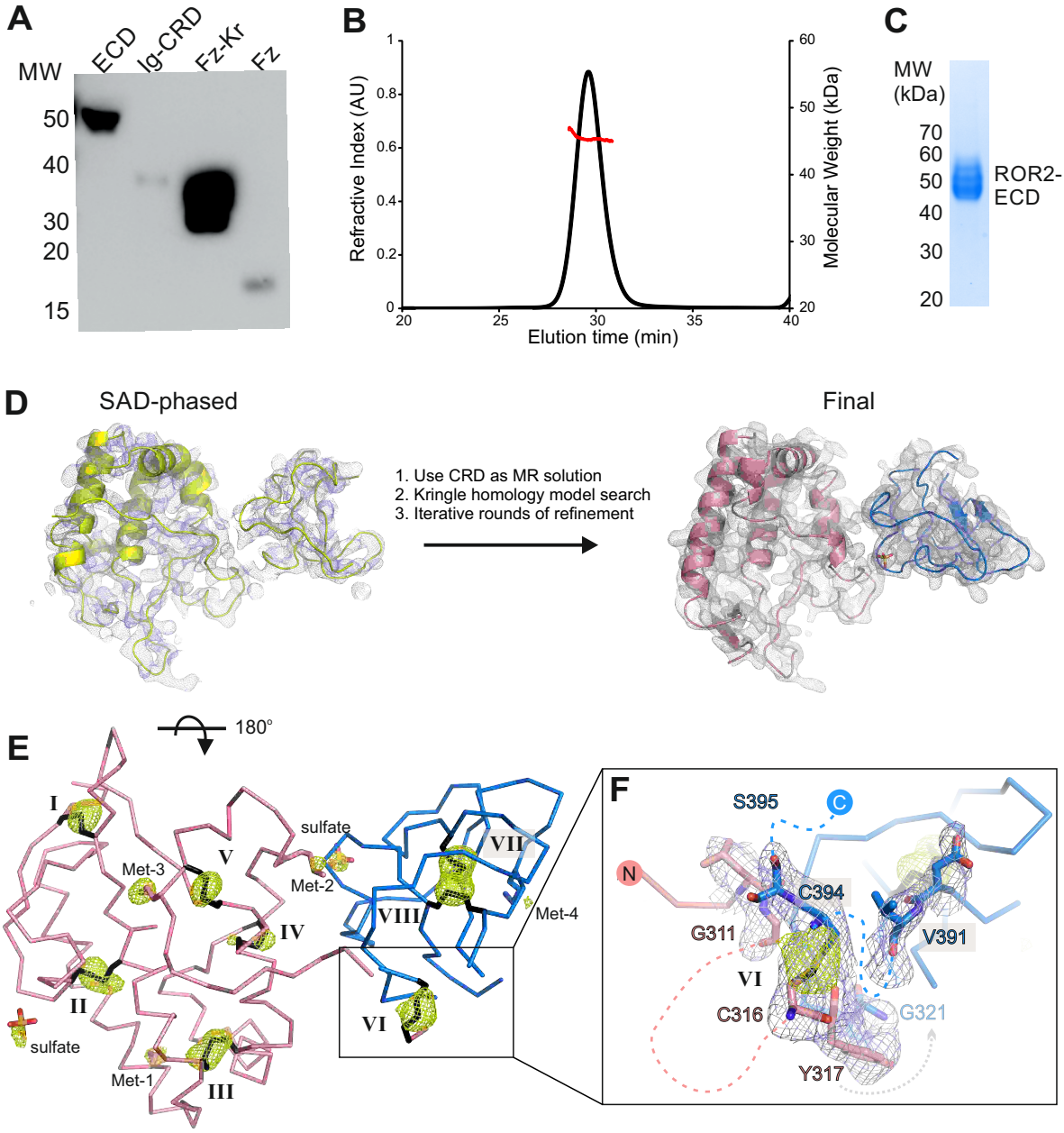

Figure 2

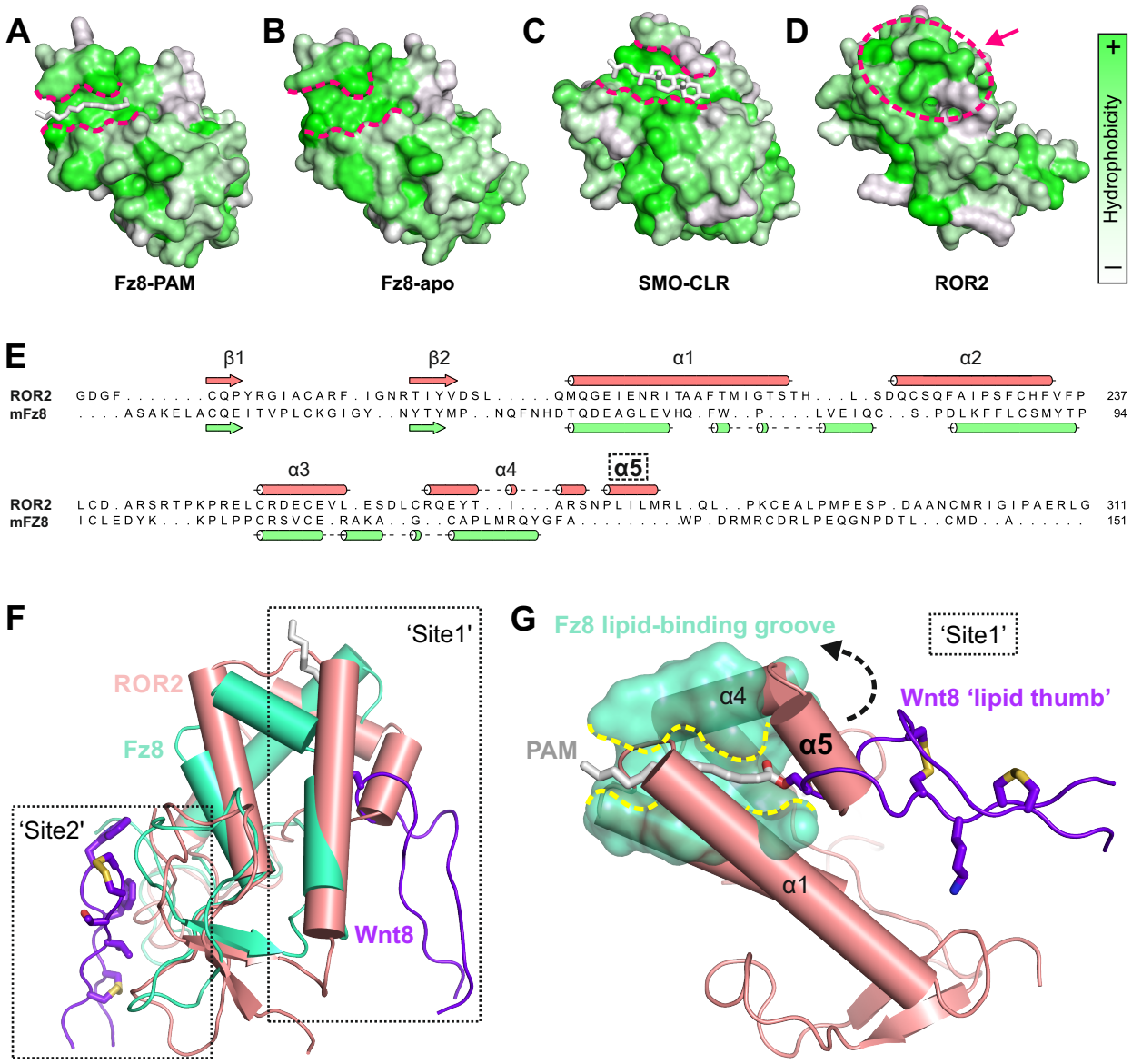

Figure S2

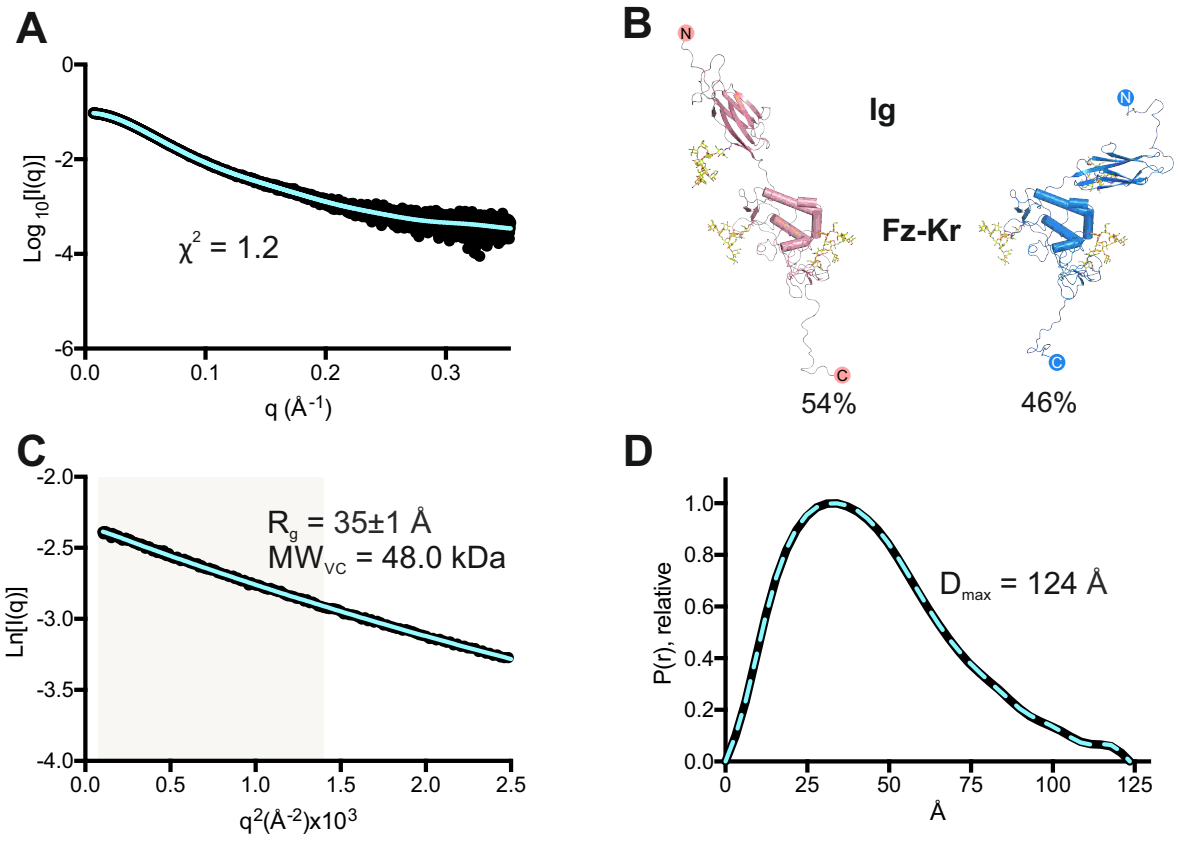

Figure 3

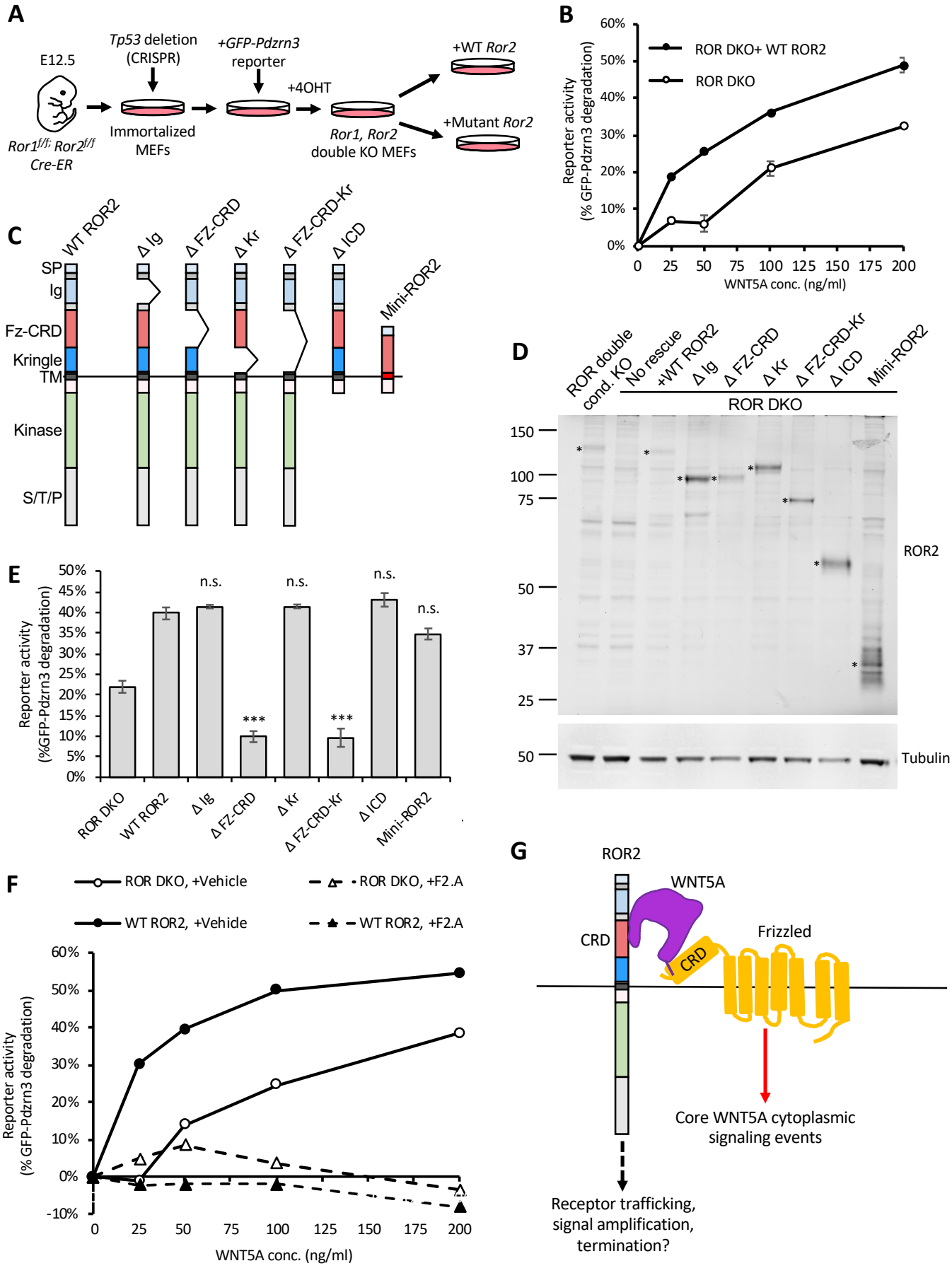

Figure 4